nature communications

Article

https://doi.org/10.1038/s41467-026-74848-6

Electric field tunable coupling strength and quantum metric hot spots in a moiré flatband superconductor

Received: 17 November 2025

Accepted: 15 June 2026

Published online: 04 July 2026

Check for updates

Le Liu[1,2,7], Yu Hong[1,2,7], Cheng-Ping Zhang[3,7], Jundong Zhu[1,2], Jingwei Dong[1,2], Kenji Watanabe[4], Takashi Taniguchi[5], Luojun Du[1,2], Dongxia Shi[1,2,6], K. T. Law[3], Guangyu Zhang[1,2,6] & Wei Yang[1,2,6]

Alternating twisted multilayer graphene presents a compelling multiband system, with a coexistence of Dirac bands and flat bands, for exploring superconductivity. However, the roles of flat bands and Dirac bands played in determining the superconductivity remain elusive. Here, we focus on the alternating twisted quadralayer graphene to reveal unconventional superconducting behaviors. We disentangle Dirac bands and flat bands, revealing a Coulomb interaction-induced band broadening effect. We further quantify the electric-field-dependent evolution of the critical temperature and coherence length, and estimate the flat-band Fermi velocity and superfluid stiffness via critical current measurements. Our results demonstrate an electric-field–tunable coupling strength within the superconducting phase, revealing unconventional properties with vanishing Fermi velocity and large superfluid stiffness. Combined with our theoretical analysis, these observations support a picture in which displacement-field-driven hybridization between flat and Dirac-like bands enhances the quantum-metric contribution to superconductivity, offering new insight into multiband flat-band superconductivity in moiré systems.

Superconductivity is characterized by flows of condensed electron pairs with zero dissipation. To understand the superconductivity, especially the multiband superconductors with high temperature superconductivity, is of fundamental interest and great promise for modern science and technology[1,2]. Recently, moiré superlattices composed of twisted multiple atomic thin layers give birth to topological flat band systems[3], where strong correlation effects enable the observation of superconductivity[4–12] along with correlated insulators[13–19], ferromagnetism[20–22], fractional[23–25] or integer[26–28] quantum anomalous Hall effect, etc. In twisted bilayer graphene (TBG), the flat band parts are situated in moiré AA regions at a low energy, while the dispersive band parts are distributed among moiré regions at a higher energy in the band structure[29]; superconductivity is observed in a specific magic angle[4]. A more intriguing example is the alternating twisted multilayer graphene (ATMG) systems[7,8,10–12,30–32], a typical multiband system hosting dispersive and flat bands[33]. The number of Dirac cones at low energy is $N-2$, where N is the number of graphene layers. ATMG has opened new avenues to investigate robust unconventional superconductivity, hosting a widely electric field-tunable superconducting phase diagram with an enhanced critical temperature and

[1]Beijing National Laboratory for Condensed Matter Physics and Institute of Physics, Chinese Academy of Sciences, Beijing, China. [2]School of Physical Sciences, University of Chinese Academy of Sciences, Beijing, China. [3]Department of Physics, Hong Kong University of Science and Technology, Clear Water Bay, Hong Kong, China. [4]Research Center for Electronic and Optical Materials, National Institute for Materials Science, 1-1 Namiki, Tsukuba, Japan. [5]Research Center for Materials Nanoarchitectonics, National Institute for Materials Science, 1-1 Namiki, Tsukuba, Japan. [6]Songshan Lake Materials Laboratory, Dongguan, China. [7]These authors contributed equally: Le Liu, Yu Hong, Cheng-Ping Zhang. e-mail: phlaw@ust.hk; gyzhang@iphy.ac.cn; wei.yang@iphy.ac.cn

a large in-plane magnetic field that exceeds the Pauli limit[34]. The hybridization between Dirac and flat bands, tunable by electrical displacement fields, triggers significant changes in superconducting coupling strength, enabling the investigation of Bardeen-Cooper-Schrieffer (BCS) to Bose-Einstein condensate (BEC) crossover[7,12]. In addition, quantum geometry has been shown to play a crucial role in flatband superconductivity[35]. Despite these efforts, it remains unclear how the flat-band and Dirac-band sectors separately contribute to superconductivity in ATMG and whether displacement-field-driven hybridization between them can enhance superconductivity through quantum geometry.

Here, we focus on the superconductivity in alternating twisted quadralayer graphene (ATQG) with a twisted angle of 1.58°. As a member of the ATMG family, ATQG is an ideal candidate to investigate the superconductivity in multi-band systems, containing two Dirac cones and two flat bands at low energy. We disentangle the carrier contributions from the flat-band and Dirac-band sectors and reveal strong interaction-induced band broadening by analyzing Landau fan diagrams and Hall response. We further quantify the displacement-field dependence of the coupling strength and superfluid stiffness. Combined with theoretical calculations, our results support a picture in which displacement-field-driven hybridization between flat and Dirac-like bands generates quantum-metric hotspots, thereby strengthening superconductivity at intermediate fields. These findings establish ATQG as a tunable multiband platform for studying the interplay of Coulomb interaction, band hybridization, quantum geometry, and flat-band superconductivity.

Results

Robust superconductivity in ATQG system

The ATQG sample is fabricated by using the 'cut and stack' method[36]. The four monolayer pieces, cut from one large flake of monolayer graphene, are alternately stacked with a relative twisted angle θ (Fig. 1a), resulting in a single moiré unit cell with the size defined by θ. In ATQG, two Dirac-type bands, located at the corner of moiré Brillouin zone K_s and K_s', respectively, coexist with the flat bands[33,37], as shown in Fig. 1b. These Dirac bands are independent from the flat bands at interlayer potential energy $U = 0$, while they hybridize with the flat bands at $U \neq 0$ with a gap opening at CNP (Fig. 1c). Figure 1d exhibits a typical longitudinal resistance (R_{xx}) map as a function of the total filling factor υ_{tot} and the displacement field D at a base temperature of $T = 30$ mK. Here, we define $\upsilon_{tot} = \upsilon_{flat} + \upsilon_{Dirac} = 4n/n_0$, where υ_{flat} and υ_{Dirac} correspond to the filling factor of the flat band and Dirac bands, respectively. The full filling carrier density n_0 is extracted from the full filling resistance peak at $U \neq 0$ where hybridization eliminates the discrepancy between υ_{tot} and υ_{flat}. It shows $n_0 = 5.78 \times 10^{12}$ /cm^2, corresponding to a twisted angle of 1.58°, where the bandwidth of the flat band is ~10 meV in continuum model calculations (Fig. 1b).

We observe robust superconductivity in a wide range of the phase diagram in Fig. 1d, indicated by the two large blue-colored regions with zero resistance spanning from υ_{tot} ~ ±2 to ~ ±4 and within a finite $|D|$ <~ 0.5 V/nm. As shown in Fig. 1e, f, the resistance in these regions quickly drops to zero when the temperature is lower than 1 K. At a fixed $\upsilon_{tot} = 2.31$, the temperature-dependent resistance exhibits a typical non-linear superconducting transition with T_c of ~1.2 K at $D = 0$ V/nm and of ~2 K at $D = 0.26$ V/nm. Notably, as shown in Fig. 1g, the temperature-dependent voltage-current (V-I) curves show a clear Berezinskii−Kosterlitz−Thouless (BKT) transition at the critical temperature of $T_{BKT} = 1.1$ K, where V is proportional to I^3, demonstrating the 2D superconducting nature in ATQG[38,39]. Furthermore, evidence of phase coherence is revealed in the magnetic field response of differential resistance dV/dI, showing a weak interference pattern and a strong suppression at the critical magnetic field $B_\perp$ ~ 0.1 T (inset of Fig. 1e). All the above-mentioned observations indicate these zero

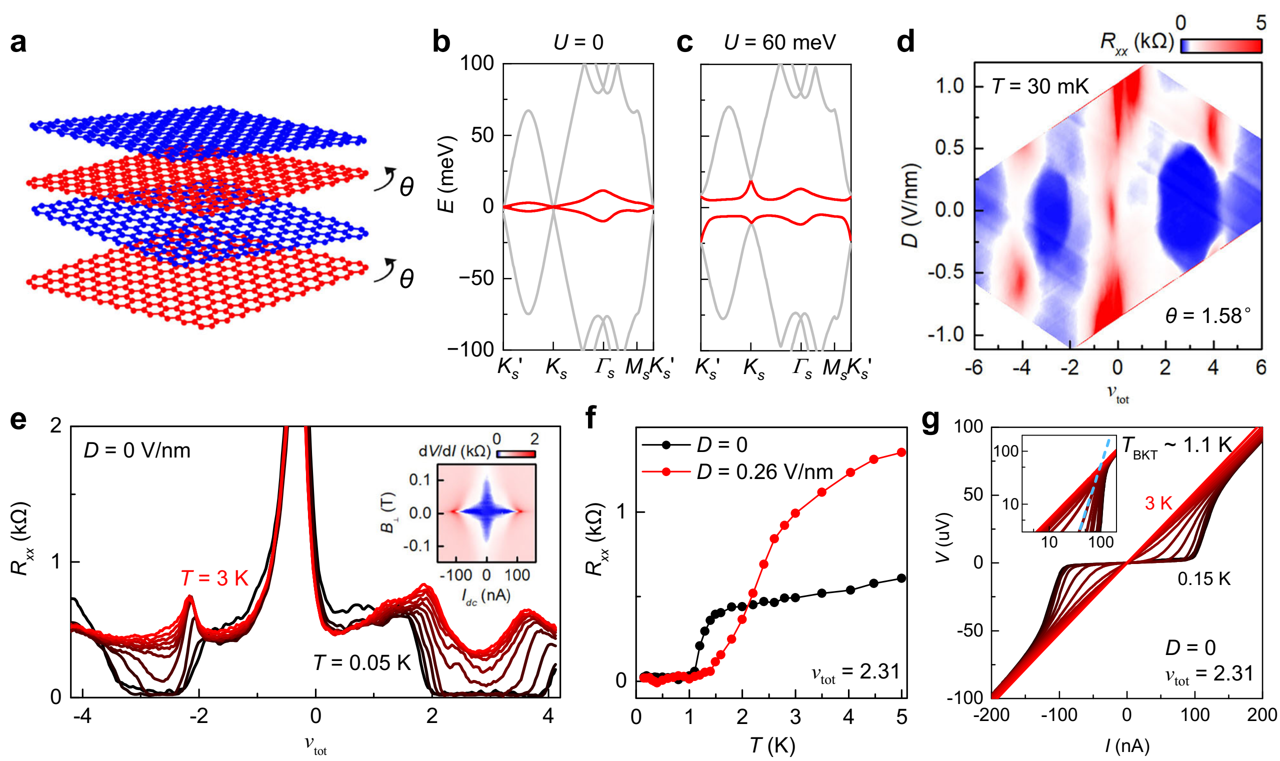

Fig. 1 | Superconductivity in alternating twisted quadralayer graphene. **a** Schematics of the stacking order of ATQG. **b**,**c** Band structures calculated from the continuum model at $U = 0$ and $U = 60$ meV. **d** R_{xx} as a function of υ_{tot} and D at $T = 30$ mK and $B = 0$ T. **e** R_{xx} versus υ_{tot} from $T = 0.05$ K to 3 K at $D = 0$. Inset, dV/dI as a function of I_{dc} and B at $\upsilon_{tot} = 2.31$ and $D = 0$. **f** R_{xx} vesus T at $D = 0$ and 0.26 V/nm. **g** V versus I from $T = 0.15$ K to 3 K. Inset, zoom-in figure in log-log coordinates. The blue dashed line is the nonlinear fitting of V ~ I^3.

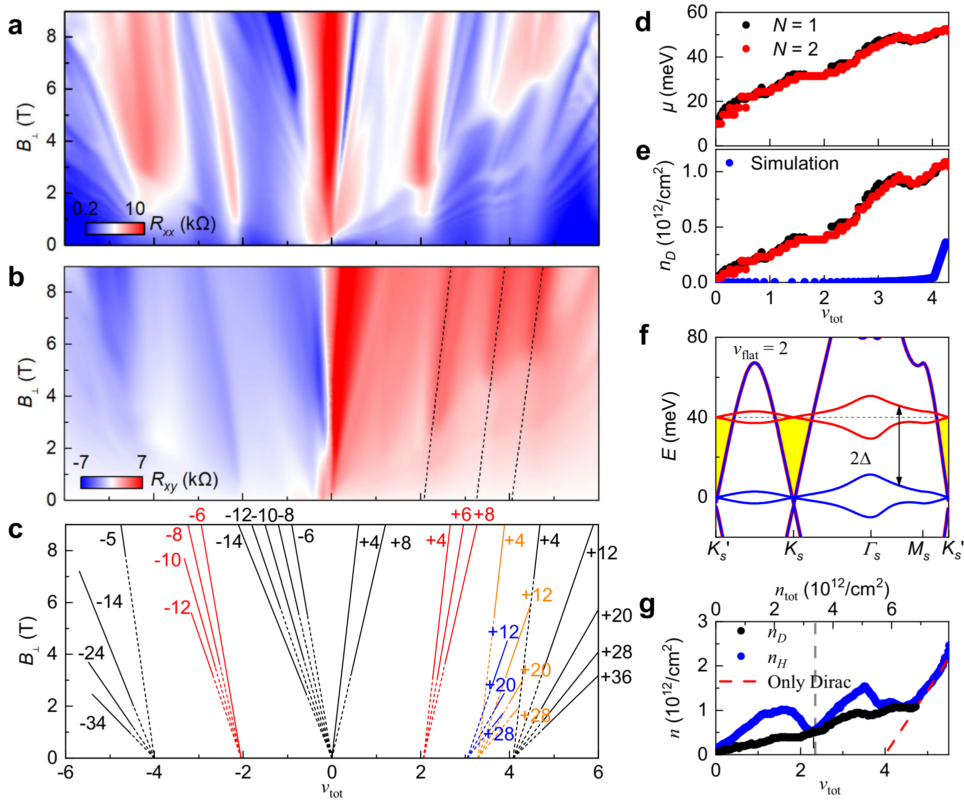

Fig. 2 | Coexistence of flat and Dirac bands. a–c Landau fan diagrams at $D = 0$ and $T = 1.7$ K. **d** μ versus ν_{tot} of $N = 1$ and 2 LL from the Dirac band. **e** n_{Dirac} verus ν_{tot} of $N = 1$ and 2 LL from the Dirac band. The blue dot line is simulated carrier densities of Dirac bands. **f** Band structure of the ATQG near $\nu_{flat} = 2$, where an isospin polarization is established due to the correlation effect. The dashed line indicates the chemical potential at 40 meV. The yellow shaded region marks the filled Dirac bands. $\Delta_{HF} = 20$ meV accounts for the flavor polarization at $\nu_{flat} = 2$. **g** Carrier densities versus ν_{tot}. The gray dashed line corresponds to $\nu_{flat} = 2$. The red dashed line corresponds to the fitting curve of $n = (\nu_{tot} - \nu_0)\, n_0/4$.

resistance states in the phase diagram are robust superconducting states.

Coexistence of Dirac and flat bands at $D = 0$

Compared with TBG, the involvement of Dirac bands extends the regime of superconductivity and simultaneously introduces complexity into the phase diagram[7,8,10–12]. Before investigating the mechanism of superconductivity in ATQG, it is crucial to disentangle the transport behaviors for the two types of bands and elucidate the respective contributions to carrier densities, which can be probed from the Landau fan diagram (Supplementary Note 3).

Figure 2a–c show Landau fan diagrams at $D = 0$. On the conduction band side ($\nu_{tot} > 0$), three sets of Landau level (LL) sequences, each starting from the LL filling factor (Chern number) $\nu_{LL} = +4$, emerge from $\nu_{tot} \sim 2$, ~3.3, and 4, respectively. The extraction details of Chern number and the band filling factor are presented in Supplementary Note 2. The $\nu_{LL} = +4$ LLs, clearly visible in the Hall resistance map of Fig. 2b (also see Supplementary Fig. 2), arise from the quantization of two Dirac bands within a topologically trivial gap in the flat band. Additionally, two sequences of higher LLs with indexes of +12, +20, and +28 are observed emanating from $\nu_{tot} = 3$ and 3.3 (see details in Supplementary Fig. 3), which is consistent with a doubling of the LL index structure expected from a single Dirac band (i.e., +6, +10, +14). At $\nu_{tot} > 4$, another LL sequence with $\nu_{LL} = +4$, +12, +20, +28, +36 appears, suggesting the exclusive contribution from Dirac bands to the LL spectrum in this regime. The emergence of LLs from nonzero filling factors suggests interaction-induced energy gaps[40].

We quantitatively extract the chemical potential and carrier density of Dirac bands[7,30] based on the trajectories of the R_{xx} maxima (Supplementary Fig. 4) where the chemical potential lies within the Nth LL of Dirac bands. The chemical potential difference between the Nth LL ($N_{LL} > 0$ for the conduction band) and the zeroth LL is expressed as $\mu_N - \mu_0 = v_F\sqrt{2e\hbar N_{LL} B}$, where v_F is the Fermi velocity of Dirac bands and $\hbar$ is the reduced Planck constant. According to the continuum model, v_F is renormalized to ~6.1×10^5 m/s. The carrier density of Dirac bands is given by $n_{Dirac} = 2N_{LL} \times 4eB/h$. Using the extracted chemical potential values from the $N_{LL} = 1$ and $N_{LL} = 2$ trajectories (Fig. 2d), we estimate the bandwidth of the flat band to be ~50 meV, significantly larger than the ~10 meV predicted by the continuum model. This large discrepancy suggests the flat band is non-rigid, where strong electron-electron interactions induce a band broadening effect through the formation of many-body energy gaps[41]. In Fig. 2e, the carrier density contributed by Dirac bands is ~ 0.96×10^{12} /cm^2 at $\nu_{tot} = 4$, one order larger than the single particle simulation prediction. This again supports the presence of substantial band broadening due to interactions.

Furthermore, both the chemical potential and carrier density remain nearly constant from $\nu_{tot} \sim 1.35$ to $\nu_{tot} \sim 2.04$, indicating the flat band is highly compressible within this doping range. Subsequently, both the chemical potential and carrier density increase rapidly for $\nu_{tot} >\sim 2.04$ ($\nu_{flat} \sim 1.76$), suggesting the onset of an interaction-driven cascade transition, where the internal symmetry (spin/valley) is broken and the symmetry-broken sub-flat-band (isospin polarized) starts to fill again, along with Dirac bands. To account for interaction effects[42–45], we introduce an isospin polarization energy near half filling (Fig. 2f). At $\nu_{flat} = 2$, the Hartree interaction (Coulomb repulsion energy) raises the flat band relative to the Dirac bands, leading to an increased carrier occupation in the latter. Meanwhile, the Fock interaction (exchange energy) splits the isospin sub-bands with an energy shift of

https://doi.org/10.1038/s41467-026-74848-6

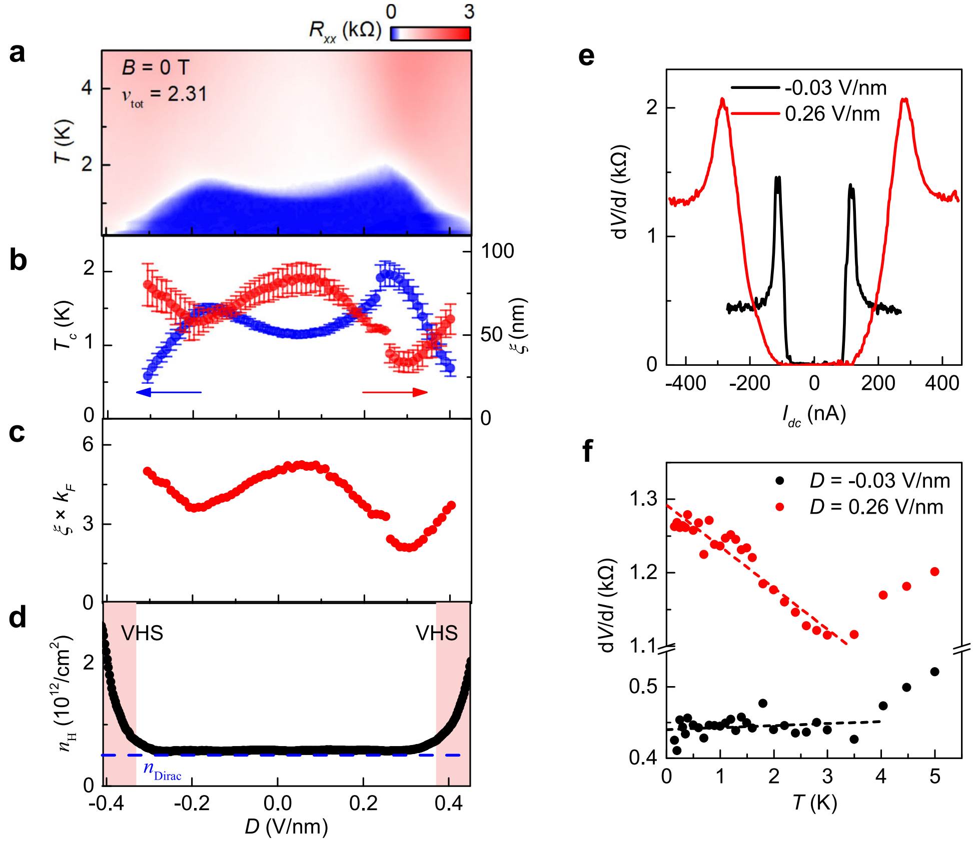

Fig. 3 | *D* tunable coupling strength of superconductivity. a R_{xx} as a function of *D* and *T* at $\upsilon_{tot} = 2.31$. **b** T_c and ξ versus *D*. The value is extracted at 40% of the normal-state resistance, with the error bar determined from the 30–50% range. **c** $\xi \times k_F$ versus *D*. **d** n_H versus *D*. The blue dashed line corresponds to the carrier density of Dirac bands. The pink regions are in the vicinity of VHS. **e** d*V*/d*I* versus I_{dc} at different *D*. **f** d*V*/d*I* versus *T*. The data is measured at $I_{dc} = 265$ (420) nA and $D = -0.03$ (0.26) V/nm.

$2\Delta_{HF} = 40$ meV. This picture effectively reproduces the substantial carrier occupations of the Dirac bands and the isospin-polarized state at $\upsilon_{flat} = 2$.

The distinction between υ_{flat} and υ_{tot} is further supported by Hall resistance measurements. As shown in Supplementary Fig. 6a, two regions of maximum Hall resistance appear near $\upsilon_{tot} = \pm 2$ at low displacement fields, marked by yellow dashed lines. These maxima indicate that the Hall carrier density, given by $n_H = B/(eR_{xy})$, resets to almost zero, consistent with a cascade transition of the flat band near half filling. Assuming minimal complexity, we regard the Hall carrier density as an estimate of the real carrier density. As shown in Fig. 2g, n_H almost equals to n_{Dirac} at $\upsilon_{tot} = 2.3$ ($\upsilon_{flat} = 1.94$), implying that the flat band contributes negligible free carriers near half filling due to the symmetry-breaking cascade transition. Beyond full filling ($\upsilon_{tot} > 4$), the Hall carrier density follows a linear relation with the doping level, $n_H = (\upsilon_{tot} - \upsilon_0)\, n_0/4$, suggesting the carrier density is exclusively contributed by Dirac bands in this regime.

Electrical field tunable coupling strength of superconductivity

To explore the superconductivity in this multi-band system, we apply a displacement field *D* to introduce band hybridization and investigate its effect on the coherent length and critical temperature. Figure 3a exhibits the superconducting phase diagram as a function of *D* at $\upsilon_{tot} = 2.31$. By applying *D* from 0 to 0.25 V/nm, the superconductivity is enhanced with T_c rising from 1.2 to 2 K; further increasing *D*, T_c decreases and eventually vanishes at $D > \sim 0.4$ V/nm. To quantitatively estimate the coupling strength of Cooper pairs in the superconducting phase, we compare the superconducting coherence length and inter-particle distance *d*. The Ginzburg – Landau (G-L) coherence length ξ is extracted from the critical magnetic field, i.e., $\xi = \sqrt{\Phi_0/(2\pi B_{c0})}$, where $\Phi_0 = h/(2e)$ is the superconducting flux quantum and B_{c0} is the critical magnetic field extrapolated to the zero-temperature limit. The measured G-L coherence length ξ shows an inverse trend of T_c, reaching a minimum ξ of ~30 nm at $D = 0.25$ V/nm (Fig. 3b). The inter-particle distance *d* is approximated as inversely proportional to the Fermi vector k_F, i.e., $1/d \sim k_F = \sqrt{4\pi n^*/g}$, where n^* is the pairing carrier density and $g = 2$ is the band degeneracy by considering the symmetry breaking at half filling. We define n^* or equivalently υ^* as $\upsilon^* = |\upsilon_{flat} - 2|$, where υ^* is measured relative to the half filling of the flat band. Figure 3c shows the product of ξ and k_F, which characterizes the ratio of the coherence length to the inter-particle distance and thus serves as a metric for the coupling strength. $\xi \times k_F$ remains below 6 across the entire *D* range and reaches a minimum of 2 at $D = 0.25$ V/nm, suggesting the superconductivity is modulated within a narrow regime close to the BEC limit[46].

The strongly coupled superconductivity modulated by *D* exhibits unconventional behaviors. As shown in Fig. 3d, n_H extracted at $B_\perp = 0.5$ T (where superconductivity is fully suppressed), remains constant for $|D| < 0.3$ V/nm and then diverges rapidly. This divergence in n_H suggests an enhanced DOS near a van Hove singularity (VHS). However, T_c decreases, and the coupling strength weakens for $|D| > 0.3$ V/nm. This observation is contrary to conventional BCS expectations. Furthermore, the d*V*/d*I* curves in Fig. 3e reveal a higher critical current at finite *D* compared to $D = 0$, suggesting a stronger coupling superconductivity approaching the BEC regime. The negative temperature-dependent behavior of d*V*/d*I* (Fig. 3f) in the normal state above critical current deviates from the conventional metal behavior. The strong correlation between electrons potentially leads to a pseudo

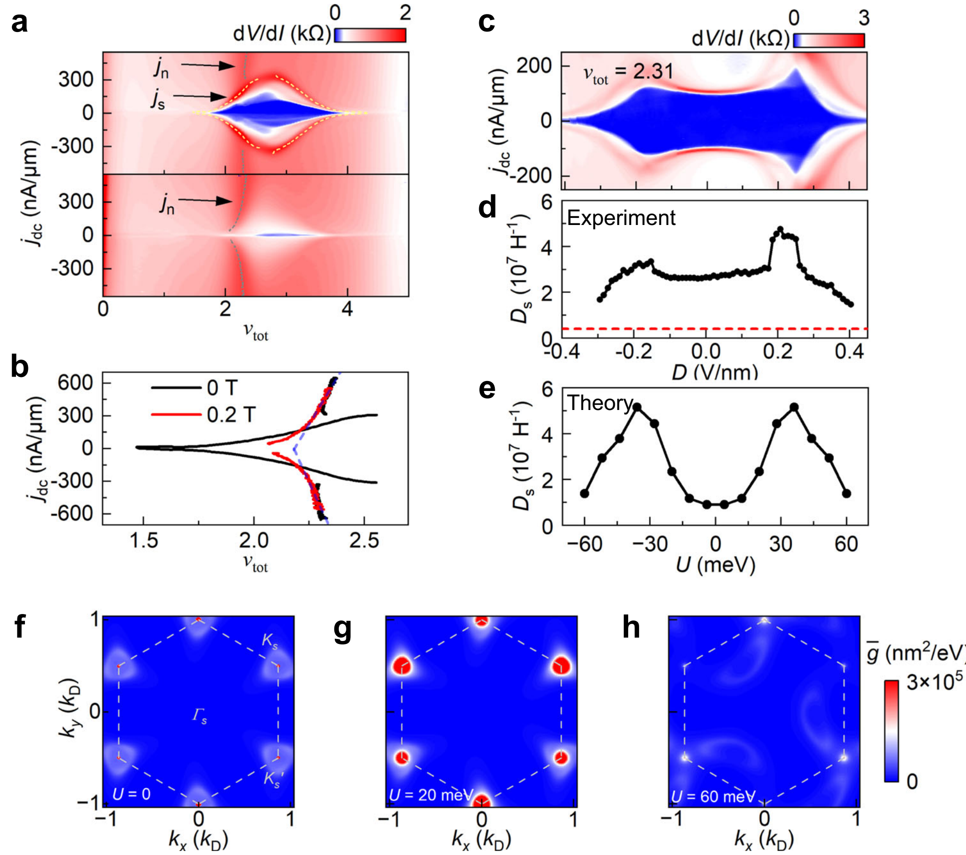

Fig. 4 | Critical currents and superfluid stiffness. a dV/dI as a function of ν_{tot} and I_{dc} at $D = 0.26$ V/nm. Top, $B = 0$ T. Bottom, $B_\perp = 0.2$ T. **b** Extracted critical currents for superconductivity and correlated insulator. Blue dashed lines are linear fitting curves. **c** dV/dI as a function of D and I_{dc} at $\nu_{tot} = 2.31$. **d** Extracted superfluid stiffness versus D. The red dashed line corresponds to the conventional contribution extracted at $D = 0.26$ V/nm for reference. **e** Theoretical calculation of superfluid stiffness at different U. **f**–**h** Momentum space distribution of the quantum metric at $U = 0$ (**f**), $U = 20$ meV (**g**) and $U = 60$ meV (**h**). g is the trace of the quantum metric tensor. k_D is the momentum difference between K_s and K_s' valleys in the moiré Brillouin zone.

energy gap of pre-paired electrons[12]. However, further experiments and theoretical investigations are needed to fully understand this phenomenon.

Critical currents and superfluid stiffness

We further quantify the superconducting properties through critical current measurements. Doping-dependent dV/dI maps at $D = 0.26$ V/nm reveal two distinct boundaries characterized by different critical currents (Fig. 4a, b). The lower boundary j_s vanishes with increasing perpendicular magnetic field, indicating its association with the superconducting critical current. In contrast, the upper boundary j_n remains evident even at higher magnetic fields. Importantly, we can quantify the superfluid stiffness, the resistance of supercurrent against the phase variation, at zero temperature limit using the critical current density j_s according to the formula $D_s = \frac{2\pi j_s}{\Phi_0 \nabla\theta_{sc}}$[35] (See Methods), where $\nabla\theta_{sc}$ is the gradient of the phase of the superconducting wavefunction. At the critical supercurrent density below T_c, superconductivity is destroyed by vortex-antivortex pairs, similar to the BKT transition at the critical temperature. The phase variation can be approximated by coherence length via $\nabla\theta_{sc} \sim 1/\xi$. Then, the experimentally observed superfluid stiffness is the product of the measured critical current density and measured Landau-Ginzburg coherence length, $D_s = \frac{2\pi j_s \xi}{\Phi_0}$.

Figure 4d shows the estimated superfluid stiffness from the measured critical supercurrent density in Fig. 4c. D_s has a nonmonotonic dependence on D, and it reaches the maximum of ~ 4×10^7 /H around $D = 0.26$ V/nm. The D_s maxima is one order larger than the conventional contribution of $D_s = \frac{e^2 n^*}{m^*}$ (the red dashed line in Fig. 4d), where $m^* = \hbar k_F / \nu_F$ is the effective mass of the flatband[35]. Note that we could also approximate the flatband Fermi velocity ν_F from the linear dependence between the non-superconducting critical current density j_n and carrier density n in Fig. 4b, which could be assigned to the critical behavior of a correlated gap at half filling due to the intraband transitions and the interband Zener-Klein tunneling[35,47–49]. The resulting value $\nu_n \approx 1700$ m/s suggests a flat band condition at the Fermi level near $\nu \sim 2$, comparable to that observed in magic angle TBG[35].

Discussion

The enhanced coupling strength and superfluid stiffness tuned by D can be attributed to the increasing contribution from the quantum metric. In flat band superconductivity, quantum metric contributions are comparable to or even larger than conventional contributions[50–52], and can be further amplified by the band touching in multiband systems[53]. As shown in Fig. 4f–h, we calculate quantum metric contributions at $\nu_{flat} = 2$. The interlayer potential (U) hybridizes the flat band and Dirac bands at K_s and K_s' points, and simultaneously, it generates hot spots of quantum metrics. As a result, the quantum metric can be enhanced at intermediate displacement fields (Fig. 4g), owing to the band hybridization. To compare with experiment quantitatively, we further calculate the superfluid stiffness, $D_s = \left(\frac{2\pi}{\Phi_0}\right)^2 \chi_{qm} \Delta^2$ (details in Supplementary Note 12), where χ_{qm} is determined by the weighted average of the quantum metric, $\triangle$ is the superconducting gap (Supplementary Fig. 15). As shown in Fig. 4e, D_s reaches a maximum of ~5×10^7 /H at finite U, consistent with the enhanced superfluid stiffness observed experimentally (Fig. 4d). Further increases in the displacement field would result in a deviation from the flatband condition and also shift the quantum metric hotspots above the Fermi energy, leading to a decrease in superfluid stiffness at high displacement fields as observed experimentally. This agreement between experiment and theory establishes an intimate connection between quantum metric effect and flat band superconductivity, and it further highlights an important role played by Dirac bands in stabilizing multiband superconductivity via generating quantum metric hot spots.

In addition, as shown in Supplementary Fig. 10, the ratio between onset temperature T^* and T_{BKT} increases from 1.45 to 2.19 with D, supporting the emergence of strong coupling associated with the quantum metric[54] at large D. Notably, measurements of the superfluid stiffness provide direct insight into the nature of the superconducting order parameter[55,56]. Recent kinetic inductance measurements also reveal possible nodal superconductivity in ATMG[57] and the indispensable contribution of quantum metric to superfluid stiffness in TBG[58].

In conclusion, we investigate unconventional superconductivity in a field-tunable multi-band system and clarify the distinct roles of flat and Dirac bands. Remarkably, the strong coupling superconductivity emerges near the half-filling of the flat band and can be enhanced by applying displacement fields. Moreover, we reveal the unconventional superconductivity with vanishing Fermi velocity and large superfluid stiffness, which goes beyond the conventional BCS prediction and is consistent with a substantial quantum metric contribution that is enhanced by displacement field-driven hybridization between the Dirac and flat bands. Our findings provide new insights into the nature of superconductivity and the BCS-BEC crossover in multiband systems, with broader implications for engineered quantum materials.

Methods

Device fabrication

The alternating twisted quatralayer graphene (ATQG) sample is fabricated into the dual gate Hall bar device with a Ti/Au top gate and a graphite bottom gate. The device is 1D contacted with Cr/Au 3/30 nm after etching with a CHF_3/O_2 mixture.

Device characterization

Two gates configuration allows us to independently tune the carrier density n and the displacement field D as $n = (C_b V_b + C_t V_t)/e$ and $D = (C_b V_b - C_t V_t)/2\varepsilon_0$, where C_b (C_t) is the geometrical capacitance per area for bottom (top) gate, V_b (V_t) is the voltage applied on the bottom (top) gate, e is the electron charge, and ε_0 is the vacuum permittivity.

The cryogenic magneto-transport measurements are mainly carried out in Leiden dilution refrigerator CF-CS81 with a magnet of 14 T and an attocube sample stage with vertical and horizontal rotation axes, and a helium-4 bath cryostat with a magnet of 9 T. We measure the four-terminal longitudinal resistance R_{xx} and Hall resistance R_{xy} using the lock-in amplifier LI5650 with a frequency of 7 ~ 20 Hz. Excitation currents are between $I = 1$ ~ 10 nA with a large series resistance of 100 MΩ. The dV/dI measurements are carried out with a combination of an AC signal (~2 nA) and a DC signal (up to ~ 650 nA).

Estimation of superfluid stiffness

In a superconductor, the superconducting current density (j) is given by $j = \frac{2\pi j_s}{\Phi_0 \nabla\theta_{sc}}$, where D_s is the superfluid stiffness and $\nabla\theta_{sc}$ is the gradient of the phase of the superconducting wavefunction. The parameter D_s quantifies the material's resistance to changes in the superconducting phase. For conventional BCS superconductors, it is defined as: $D_{s,conn} = e^2 n^*/m^*$, where n^* is the pairing carrier density and m^* is the effective mass. The effective mass can be calculated with the formula $m^* = \hbar k_F/v_F$, where $k_F = \sqrt{2\pi n^*}$ is the Fermi wave vector, and v_F is the Fermi velocity. For multiband superconductors with topological bands, D_s is the sum of both the conventional contribution and the one from quantum metric due to the non-localization of Wannier functions[59], i.e., $D_s = D_s$ (conventional) + D_s (geometric).

In our study, we can quantify the conventional contribution from the measured carrier densities from the Dirac spectroscopy method and the Fermi velocity estimated via the drift velocity v_n that is determined from the critical current density $j = nev_n$ near $\nu = 2$ above the superconducting regime. For conventional metals, the drift velocity v_{drift} depends on the scattering time, and it usually saturates at a value much smaller than the Fermi velocity v_F, limited by optical phonons and other scattering mechanisms. For a small gap 2D semimetals or semiconductors, scattering also depends strongly on the Fermi surface when the Fermi level is close to the gap (for details, please see the inset of Fig. 2b in ref. 47 and related discussions in literature[35,47,48]). In addition, the flatband Fermi velocity is greatly reduced, which makes it easier to enter the drift velocity saturation regime. In our experiments, the second critical current occurs near the correlated gap at half filling of the flatband, and it scales linearly with carrier density, indicating a fixed critical velocity (on the order of 1000 m/s) across different carrier densities. These observations are expected for the flatband transport in the saturated regime, where the critical velocity saturation is limited by the Fermi velocity of the band structure. The calculated $v_n = 1700$ m/s is three orders smaller than that in monolayer graphene and is of the same order of magnitude compared with those in magic angle TWG[35] and alternating twisted multilayer graphene[57].

Under flat-band conditions, the conventional contribution to D_s is minimal, while the geometric component−arising from the quantum metric−dominates the superfluid stiffness. We can determine the overall D_s from experimental measurements. At the depairing current $j = j_s$, the superconducting phase gradient satisfies $\nabla\theta_{sc} \approx 1/\xi$. Substituting this into the definition of superfluid stiffness yields $D_s = 2\pi j_s \xi/\Phi_0$, where ξ is the G-L coherent length, and Φ_0 is the superconducting flux quantum. Hence, with the critical parameters of j_s and ξ, we can calculate D_s.

Data availability

The data generated in this study are provided in the Source Data file. Source data are provided with this paper.

References

1. Zhou, X. et al. High-temperature superconductivity. *Nat. Rev. Phys.* **3**, 462–465 (2021).
2. Molodyk, A. & Larbalestier, D. C. The prospects of high-temperature superconductors. *Science* **380**, 1220–1222 (2023).
3. Bistritzer, R. & MacDonald, A. H. Moiré bands in twisted double-layer graphene. *Proc. Natl. Acad. Sci. USA* **108**, 12233–12237 (2011).
4. Cao, Y. et al. Unconventional superconductivity in magic-angle graphene superlattices. *Nature* **556**, 43–50 (2018).
5. Lu, X. et al. Superconductors, orbital magnets and correlated states in magic-angle bilayer graphene. *Nature* **574**, 653–657 (2019).
6. Yankowitz, M. et al. Tuning superconductivity in twisted bilayer graphene. *Science* **363**, 1059–1064 (2019).
7. Park, J. M., Cao, Y., Watanabe, K., Taniguchi, T. & Jarillo-Herrero, P. Tunable strongly coupled superconductivity in magic-angle twisted trilayer graphene. *Nature* **590**, 249–255 (2021).
8. Hao, Z. et al. Electric field–tunable superconductivity in alternating-twist magic-angle trilayer graphene. *Science* **371**, 1133–1138 (2021).
9. Oh, M. et al. Evidence for unconventional superconductivity in twisted bilayer graphene. *Nature* **600**, 240–245 (2021).
10. Park, J. M. et al. Robust superconductivity in magic-angle multilayer graphene family. *Nat. Mater.* **21**, 877–883 (2022).
11. Zhang, Y. et al. Promotion of superconductivity in magic-angle graphene multilayers. *Science* **377**, 1538–1543 (2022).
12. Kim, H. et al. Evidence for unconventional superconductivity in twisted trilayer graphene. *Nature* **606**, 494–500 (2022).
13. Cao, Y. et al. Correlated insulator behaviour at half-filling in magic-angle graphene superlattices. *Nature* **556**, 80–84 (2018).

14. Cao, Y. et al. Tunable correlated states and spin-polarized phases in twisted bilayer–bilayer graphene. *Nature* **583**, 215–220 (2020).
15. Liu, X. et al. Tunable spin-polarized correlated states in twisted double bilayer graphene. *Nature* **583**, 221–225 (2020).
16. Shen, C. et al. Correlated states in twisted double bilayer graphene. *Nat. Phys.* **16**, 520–525 (2020).
17. Liu, L. et al. Isospin competitions and valley polarized correlated insulators in twisted double bilayer graphene. *Nat. Commun.* **13**, 3292 (2022).
18. Chen, S. et al. Electrically tunable correlated and topological states in twisted monolayer-bilayer graphene. *Nat. Phys.* **17**, 374–380 (2021).
19. Chen, G. et al. Evidence of a gate-tunable Mott insulator in a trilayer graphene moiré superlattice. *Nat. Phys.* **15**, 237–241 (2019).
20. Sharpe, A. L. et al. Emergent ferromagnetism near three-quarters filling in twisted bilayer graphene. *Science* **365**, 605–608 (2019).
21. Chen, G. et al. Tunable correlated Chern insulator and ferromagnetism in a moiré superlattice. *Nature* **579**, 56–61 (2020).
22. Liu, L. et al. Observation of first-order quantum phase transitions and ferromagnetism in twisted double bilayer graphene. *Phys. Rev. X* **13**, 031015 (2023).
23. Park, H. et al. Observation of fractionally quantized anomalous Hall effect. *Nature* **622**, 74–79 (2023).
24. Xu, F. et al. Observation of integer and fractional quantum anomalous Hall effects in twisted bilayer MoTe 2. *Phys. Rev. X* **13**, 031037 (2023).
25. Lu, Z. et al. Fractional quantum anomalous Hall effect in multilayer graphene. *Nature* **626**, 759–764 (2024).
26. Serlin, M. et al. Intrinsic quantized anomalous Hall effect in a moiré heterostructure. *Science* **367**, 900–903 (2020).
27. Polshyn, H. et al. Electrical switching of magnetic order in an orbital Chern insulator. *Nature* **588**, 66–70 (2020).
28. Li, T. et al. Quantum anomalous Hall effect from intertwined moiré bands. *Nature* **600**, 641–646 (2021).
29. Song, Z.-D. & Bernevig, B. A. Magic-angle twisted bilayer graphene as a topological heavy fermion problem. *Phys. Rev. Lett.* **129**, 047601 (2022).
30. Shen, C. et al. Dirac spectroscopy of strongly correlated phases in twisted trilayer graphene. *Nat. Mater.* **22**, 316–321 (2023).
31. Burg, G. W. et al. Emergence of correlations in alternating twist quadrilayer graphene. *Nat. Mater.* **21**, 884–889 (2022).
32. Phinney, I. Y. et al. Modulation of superconductivity across a Lifshitz transition in alternating-angle twisted quadrilayer graphene. *Phys. Rev. Lett.* **136**, 086501 (2026).
33. Khalaf, E., Kruchkov, A. J., Tarnopolsky, G. & Vishwanath, A. Magic angle hierarchy in twisted graphene multilayers. *Phys. Rev. B* **100**, 085109 (2019).
34. Cao, Y., Park, J. M., Watanabe, K., Taniguchi, T. & Jarillo-Herrero, P. Pauli-limit violation and re-entrant superconductivity in moiré graphene. *Nature* **595**, 526–531 (2021).
35. Tian, H. et al. Evidence for Dirac flat band superconductivity enabled by quantum geometry. *Nature* **614**, 440–444 (2023).
36. Kim, K. et al. van der Waals heterostructures with high accuracy rotational alignment. *Nano Lett.* **16**, 1989–1995 (2016).
37. Carr, S. et al. Ultraheavy and ultrarelativistic Dirac quasiparticles in sandwiched graphenes. *Nano Lett.* **20**, 3030–3038 (2020).
38. Hebard, A. F. & Fiory, A. T. Critical-exponent measurements of a two-dimensional superconductor. *Phys. Rev. Lett.* **50**, 1603–1606 (1983).
39. Xing, Y. et al. Quantum Griffiths singularity of superconductor-metal transition in Ga thin films. *Science* **350**, 542–545 (2015).
40. Xie, M. & MacDonald, A. H. Weak-field Hall resistivity and spin-valley flavor symmetry breaking in magic-angle twisted bilayer graphene. *Phys. Rev. Lett.* **127**, 196401 (2021).
41. Xie, Y. et al. Spectroscopic signatures of many-body correlations in magic-angle twisted bilayer graphene. *Nature* **572**, 101–105 (2019).
42. Bocarsly, M. et al. Coulomb interactions and migrating Dirac cones imaged by local quantum oscillations in twisted graphene. *Nat. Phys.* **21**, 421–429 (2025).
43. Xie, F., Regnault, N., Călugăru, D., Bernevig, B. A. & Lian, B. Twisted symmetric trilayer graphene. II. Projected Hartree-Fock study. *Phys. Rev. B* **104**, 115167 (2021).
44. Kolář, K., Zhang, Y., Nadj-Perge, S., Von Oppen, F. & Lewandowski, C. Electrostatic fate of N -layer moiré graphene. *Phys. Rev. B* **108**, 195148 (2023).
45. Wang, Z. et al. Kekulé spirals and charge transfer cascades in twisted symmetric trilayer graphene. *Phys. Rev. B* **109**, L201119 (2024).
46. Chen, Q., Wang, Z., Boyack, R., Yang, S. & Levin, K. When superconductivity crosses over: from BCS to BEC. *Rev. Mod. Phys.* **96**, 025002 (2024).
47. Yang, W. et al. A graphene Zener–Klein transistor cooled by a hyperbolic substrate. *Nat. Nanotech* **13**, 47–52 (2018).
48. Berdyugin, A. I. et al. Out-of-equilibrium criticalities in graphene superlattices. *Science* **375**, 430–433 (2022).
49. Schmitt, A. et al. Mesoscopic Klein-Schwinger effect in graphene. *Nat. Phys.* **19**, 830–835 (2023).
50. Hu, X., Hyart, T., Pikulin, D. I. & Rossi, E. Geometric and conventional contribution to the superfluid weight in twisted bilayer graphene. *Phys. Rev. Lett.* **123**, 237002 (2019).
51. Xie, F., Song, Z., Lian, B. & Bernevig, B. A. Topology-bounded superfluid weight in twisted bilayer graphene. *Phys. Rev. Lett.* **124**, 167002 (2020).
52. Chen, S. A. & Law, K. T. Ginzburg-Landau theory of flat-band superconductors with quantum metric. *Phys. Rev. Lett.* **132**, 026002 (2024).
53. Huhtinen, K.-E., Herzog-Arbeitman, J., Chew, A., Bernevig, B. A. & Törmä, P. Revisiting flat band superconductivity: dependence on minimal quantum metric and band touchings. *Phys. Rev. B* **106**, 014518 (2022).
54. Wang, Z., Chaudhary, G., Chen, Q. & Levin, K. Quantum geometric contributions to the BKT transition: beyond mean field theory. *Phys. Rev. B* **102**, 184504 (2020).
55. Singh, G. et al. Competition between electron pairing and phase coherence in superconducting interfaces. *Nat. Commun.* **9**, 407 (2018).
56. Mallik, S. et al. Superfluid stiffness of a KTaO3-based two-dimensional electron gas. *Nat. Commun.* **13**, 4625 (2022).
57. Banerjee, A. et al. Superfluid stiffness of twisted trilayer graphene superconductors. *Nature* **638**, 93–98 (2025).
58. Tanaka, M. et al. Superfluid stiffness of magic-angle twisted bilayer graphene. *Nature* **638**, 99–105 (2025).
59. Peotta, S. & Törmä, P. Superfluidity in topologically nontrivial flat bands. *Nat. Commun.* **6**, 8944 (2015).

Acknowledgements

We thank Fengcheng Wu (Wuhan University), Zhida Song (Peking University), Kun Jiang, Shiliang Li, and Kui Jin (Institute of Physics, CAS) for useful discussions.

Author contributions

W.Y. and G.Z. supervised the project. W.Y. and L.L. designed the experiments. L.L. and Y.H. fabricated the devices and performed the magneto-transport measurement. L.L. performed the band structure calculations. C.P.Z. and K.T.L. developed the theory for the quantum metric calculations. K.W. and T.T. provided hexagonal boron nitride crystals. L.L., C.P.Z., K.T.L., G.Z., and W.Y. analyzed the data. L.L. and W.Y. wrote the paper with input from all the authors.

Funding
This work was supported by the Beijing Natural Science Foundation (JQ25003), the National Key Research and Development Program (Grant Nos. 2020YFA0309600, 2021YFA1202900, and 2024FYA1410400), the Natural Science Foundation of China (NSFC, Grant Nos. 12074413 and 61888102), the Quantum Science and Technology-National Science and Technology Major Project (Grant No. 2025ZD0300500), the Strategic Priority Research Program of CAS (Grant Nos. XDB1710000 and 33000000), and the Key-Area Research and Development Program of Guangdong Province (Grant No. 2020B0101340001). K.T.L. acknowledges the support of the Ministry of Science and Technology, China, the New Cornerstone Foundation, the State Key Laboratory of Quantum Information Technologies and Materials, and the Hong Kong Research Grants Council through Grants No. MOST23SC01-A, No. RFS2021-6S03, No. C6053-23G, No. AoE/P-701/20, AoE/P-604/25 R, No. 16309223, No. 16311424, and No. 16300325. C.P.Z. acknowledges the support of HKRGC through JRFS2526-6S02. K.W. and T.T. acknowledge support from the Elemental Strategy Initiative conducted by the MEXT, Japan (Grant No. JPMXP0112101001), JSPS KAKENHI (Grant Nos. 19H05790, 20H00354 and 21H05233) and A3 Foresight by JSPS.

Competing interests
The authors declare no competing interests.

Additional information
Supplementary information The online version contains supplementary material available at https://doi.org/10.1038/s41467-026-74848-6.

Correspondence and requests for materials should be addressed to K. T. Law, Guangyu Zhang or Wei Yang.

Peer review information *Nature Communications* thanks the anonymous reviewers for their contribution to the peer review of this work. A peer review file is available.